Oxidation Behavior of a Spark Plasma Sintered Ti–48Al–2W–0.1B Alloy at 800 °C

Marie-Pierre Bacos[1] · Sylvain Ceccacci[1] · Jean-Philippe Monchoux[2] ·
Cécile Davoine[1] · Thomas Gheno[1] · Catherine Rio[1] · Ariel Morel[1] ·
Jean-Sébastien Merot[3] · Frédéric Fossard[3] · Marc Thomas[1]

Abstract

Spark plasma sintering (SPS) enables the manufacturing of TiAl alloys with an exceptional combination of low density and mechanical properties such as acceptable ductility at room temperature and high strength at high temperature. However, TiAl alloys are known to exhibit low oxidation resistance above 700 °C. The oxidation of a Ti–48Al–2W–0.1B (at. %) processed by SPS was investigated at 800 °C. Coupons were oxidized in air and in Ar-21O_2 (vol%), in isothermal and cyclic tests. In air, the alloy formed a mixture of Ti and Al oxides, but oxidation was slower than typically observed for W-free alloys. The oxide scale and underlying alloy were characterized by X-ray diffraction and electron microscopy in order to examine the beneficial role of W in the oxidation resistance. The main constituents of the reaction product after reaction in air may be described as follows (from gas to alloy): TiO_2/porous $Al_2O_3/TiO_2 + Al_2O_3/TiN + Al_2O_3 + W/TiAl_2 + W/TiAl$. Close examination suggests that the relatively good oxidation resistance of the alloy is related to W doping of TiO_2 in the mixed $Al_2O_3 + TiO_2$ layer. The alloy formed an Al-rich oxide scale with much slower kinetics in Ar-21O_2, confirming the detrimental role of N in the oxidation process.
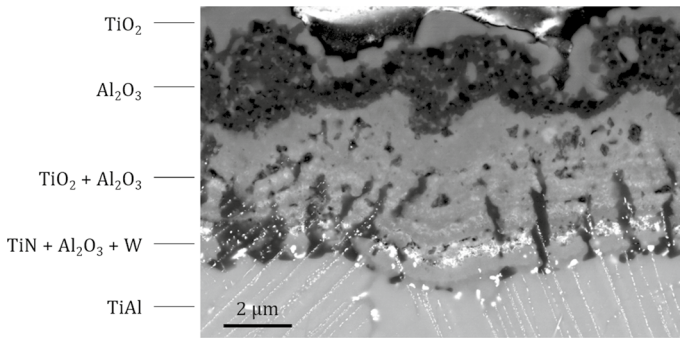
✉ Thomas Gheno
thomas.gheno@onera.fr

1 DMAS, ONERA, Université Paris Saclay, 92322 Châtillon, France

2 CEMES, CNRS UPR 8011, 29 rue Jeanne Marvig, 31055 Toulouse, France

3 LEM, UMR 104 CNRS-ONERA, Université Paris Saclay, 92322 Châtillon, France

Graphic Abstract

TiO$_2$

Al$_2$O$_3$

TiO$_2$ + Al$_2$O$_3$

TiN + Al$_2$O$_3$ + W

TiAl

2 μm

Introduction

Titanium aluminides have attracted interest in the industry thanks to the combination of low density (about half that of Ni-based superalloys) and high-temperature strength. Alloys based on γ-TiAl are now implemented for structural applications at 550–750 °C in the new generations of turbo engines. Improvements in high-temperature mechanical properties are being pursued based on alloying additions and modifications to the processing conditions, aimed at obtaining specific microstructures. The IRIS alloy (Innovative manufacturing Route for Intermetallic alloys by spark plasma net Shaping) results from such an effort: it contains W and B additions (Ti–48Al–2W–0.1B at%) and has a near-lamellar microstructure obtained via the powder metallurgy (PM) + spark plasma sintering (SPS) route [1]. Specifically, PM processing helps eliminate the macro-segregations and reduce the solidification texture, while the short densification cycle of SPS was used to limit microstructure coarsening. The processing conditions were optimized to obtain a good balance between several microstructural features and offer the best compromise in mechanical properties. This was achieved through indirect particle strengthening (grain size, dislocation substructure, etc.) rather than through precipitation hardening or solid solution strengthening. In particular, lamellar α_2/γ colonies provide high-temperature resistance, while γ bands surrounding the colonies help maintain room temperature ductility.

One current limitation to the use of γ-TiAl alloys in high-temperature applications such as turbine blades is their poor oxidation resistance above 700 °C. Indeed, instead of a continuous and dense α-Al$_2$O$_3$ layer, which would provide an effective protection, γ-TiAl alloys tend to grow mixed oxide layers resulting from the competitive oxidation of Ti and Al [2]. Additions of W, Mo or Nb have been observed to improve the oxidation resistance by decreasing the growth rate of the mixed

$Al_2O_3 + TiO_2$ layer [3]. This paper aims at studying the oxidation behavior of the IRIS alloy at 800 °C, with a focus on the role of W.

Materials and Methods

SPS densification was performed at PNF2 (Plateforme Nationale de Frittage Flash/CNRS in Toulouse, France) on a Sumitomo Dr Sinter 2080 machine. The temperature was measured by an external pyrometer at the outer wall of the die. The sample temperature was calibrated based on the β transus temperature to take into account thermal gradients in the molds. The heating rate was set to 100 K min^{-1} at the beginning and then reduced to 25 K min^{-1} for 3 min to avoid overshooting. The pressure rate was 25 MPa min^{-1}. The diameter and height of densified samples were 36 mm and 8 mm, respectively. The dwell temperature and pressure to obtain a lamellar structure were 1315 °C at the outer wall of the die (estimated temperature at the sample core: 1375 °C) and 50 MPa for 2 min. The alloy powder was made by gas atomization and obtained from Allegheny Technologies Incorporated (Pittsburgh, PA, USA).

The densified samples were cut into cylindrical (11 mm in diameter and 2 mm thick) or cuboid shape ($10 \times 15 \times 3$ mm^3) by electrical discharge machining for isothermal and cyclic oxidation, respectively, and ground with SiC paper up to a P800 grit finish. The edges of the cuboid samples were beveled to reduce stress build-up in the oxide during thermal cycling.

Isothermal oxidation was carried out in a Setaram Setsys Evolution equipped with a thermogravimetric analysis (TGA) module, operated at 800 °C with a gas flow of 30 ml/min. The samples were hung by a platinum wire. The TGA experiments were conducted in synthetic air and in Ar-21 vol. % O_2 for 100 h. The air test was duplicated to verify the repeatability, and a third air test was carried out for 240 h to reach the steady state (see "Isothermal Oxidation in Air" section).

Cyclic oxidation was conducted in a horizontal furnace for 1000 cycles in laboratory air. Each cycle consisted of a period of 70 min at 800 °C and 210 s at ambient temperature (the total duration at 800 °C is 1167 h). The sample, placed in an alumina tray, was slowly introduced and quickly removed from the hot zone of the furnace to avoid tensile thermal stress. The sample was removed, weighed and photographed every few cycles initially, and every 50 cycles thereafter.

After oxidation, the sample surfaces were analyzed by X-ray diffraction (XRD, PANalytical Empyrean diffractometer). Metallographic cross sections were then prepared and analyzed by scanning electron microscopy (SEM). Chemical compositions were measured by energy-dispersive X-ray spectrometry (EDS), while crystallographic information was obtained by electron backscatter diffraction (EBSD). All of these experiments were performed in a FEG-SEM Zeiss Merlin with an EBSD system (TSL instrumentation software and Nordiff detector) and EDS system (SAMx software and SDD detector). A thin foil was prepared from the cyclic oxidation sample by focused ion beam (FIB) milling on a DualBeam FIB-SEM Thermo Fisher Helios 660 and was then analyzed by scanning/transmission electron

Fig. 1 SEM micrograph of as-prepared IRIS alloy showing the lamellar α_2/γ grains, with a γ band and β_0 precipitates at the grain boundaries
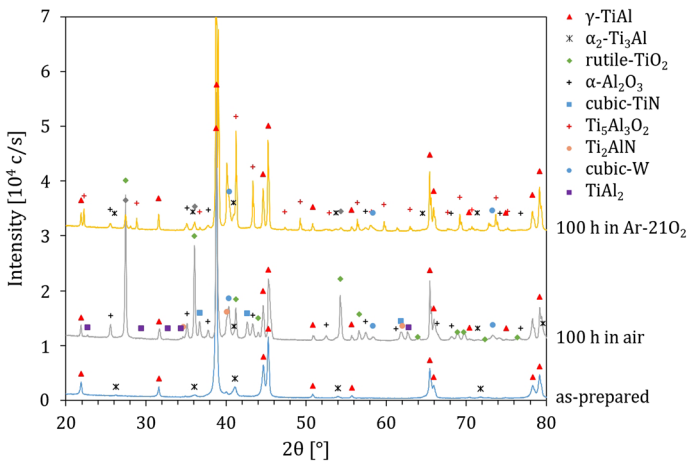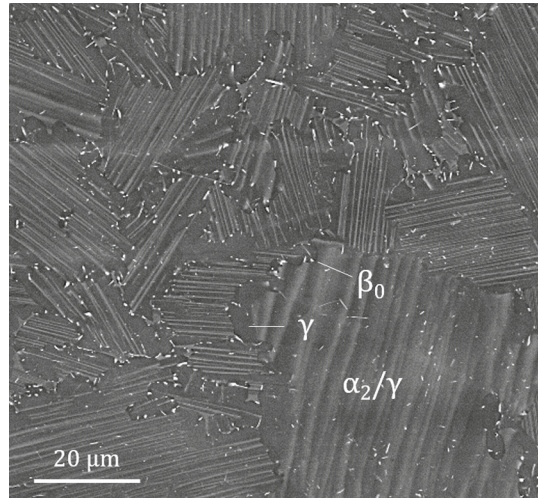
Fig. 2 XRD patterns measured on the IRIS alloy in the as-prepared state and after 100-h oxidation in air and in Ar-21O_2 at 800 °C

microscopy (S/TEM) on a STEM Zeiss Libra 200 for high-angle annular dark field (HAADF) imaging, EDS and a TEM Thermo Fisher CM20 for bright field imaging.
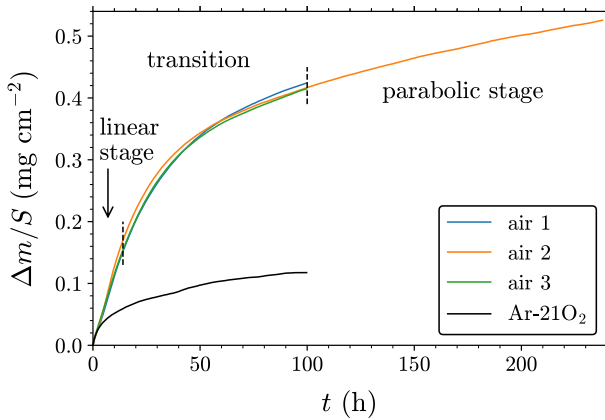
Fig. 3 Thermogravimetric analysis of the IRIS alloy at 800 °C in air and Ar-21O$_2$

Experimental Results

As-Prepared Microstructure

The microstructure of the IRIS alloy is composed of α_2/γ lamellar grains, with a γ band and W-rich β_0 precipitates at the grain boundaries, as shown in Fig. 1 (α_2, γ and β_0 refer to the D0$_{19}$ compound based on Ti$_3$Al, the L1$_0$ compound based on TiAl and the B2 compound based on TiAl, respectively). An XRD pattern is shown in Fig. 2. The average sizes of α_2/γ grains and γ band are 50 μm and 5–10 μm, respectively, whereas β_0 precipitates are up to 5 μm in length. The width of the α_2 and γ lamellae is 150–200 nm on average and the volume fraction of α_2 is about 15%. Details on the formation mechanism of the microstructure can be found in Ref. [4].

Isothermal Oxidation in Air

The isothermal oxidation kinetics measured in air at 800 °C are shown in Fig. 3. The three tests performed in air gave consistent results. The mass gain reached after 100 h is 0.4 mg cm^{-2}. In comparison, the mass gains measured after 100 h in air at 800 °C are about 0.9 mg cm^{-2} for the TNM alloy (Ti–43.5Al–4Nb–1Mo–0.1B, in at. %) [5] and 1.2 mg cm^{-2} for the GE alloy (Ti–48Al–2Cr–2Nb, in at. %) [6]. The oxidation kinetics of the IRIS alloy in air first exhibit a linear stage for about 15 h, followed by a transition stage, and eventually reach a parabolic stage after about 100 h (Fig. 3). The parabolic rate constant is determined by fitting Eq. 1 to the TGA data,

$$t = a + b\Delta m + c\Delta m^2, \tag{1}$$

where Δm is the mass gain per area at time t, and a, b and c are constants; the parabolic constant is $k_p = 1/c$ [7]. This led to a value of $k_p = 8 \times 10^{-14}$ g^2 cm^{-4} s^{-1}
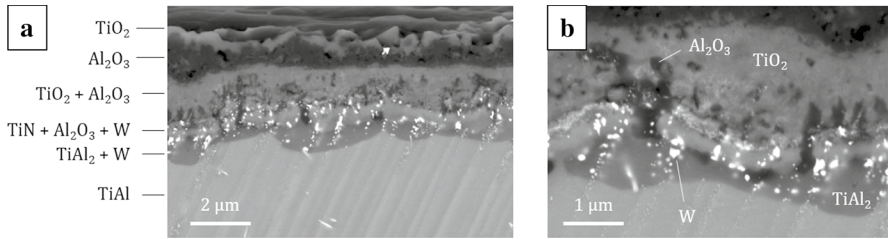
Fig. 4 SEM micrograph in backscattered electron mode (BSE) of the IRIS alloy after 100-h oxidation in air at 800 °C. **a** Overview of the oxidation products; **b** detailed view of the alloy/scale interface

in the [100 h, 240 h] time range, which is about a factor of 10 lower than values reported for TiAl-W alloys in air at 800 °C in the review by Fergus [8]. It is noted that Fergus found that a k_p of about 10^{-13} g^2 cm^{-4} s^{-1} was representative of long-term oxidation protection.

An XRD pattern obtained from one of the specimens oxidized 100 h in air is shown together with that recorded in the as-prepared state in Fig. 2. The main identified phases, in addition to γ-TiAl, are TiO_2-rutile, α-Al_2O_3, $TiAl_2$, TiN and a cubic phase that will be referred to as bcc-W (which may contain some Ti). Possible additional phases are Ti_2AlN and α_2-Ti_3Al. The XRD results were used together with SEM-EDS analysis of the cross section to determine the constitution of the oxide scale.

A cross-sectional micrograph of the same specimen is shown in Fig. 4. The outer part of the scale is composed of a thin and continuous layer of TiO_2. Underneath lies a porous Al_2O_3 layer, followed by a thick layer composed of TiO_2 and Al_2O_3 particles. A two-phase layer around 0.5 µm thick and composed of alternate TiN
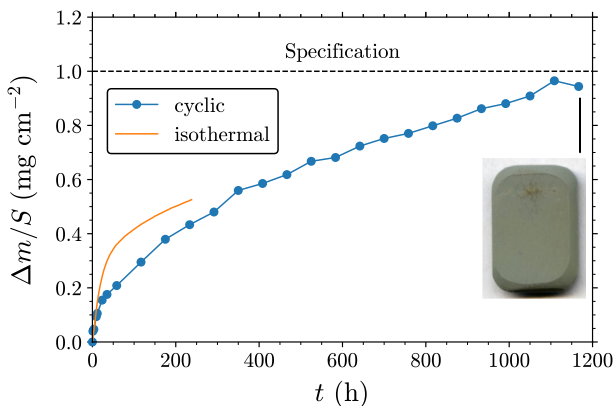
Fig. 5 Mass gains of the IRIS alloy during cyclic oxidation in laboratory air at 800 °C. The insert shows a photograph of the specimen at the end of the 1000 cycles. The mass gains measured in the 240-h isothermal TGA test are included for comparison
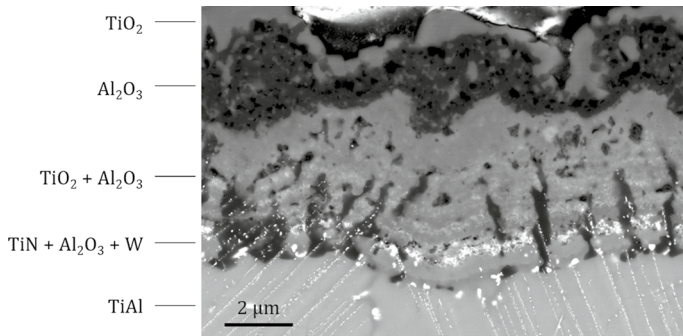
Fig. 6 SEM-BSE image of the IRIS alloy after 1000 cycles in air at 800 °C
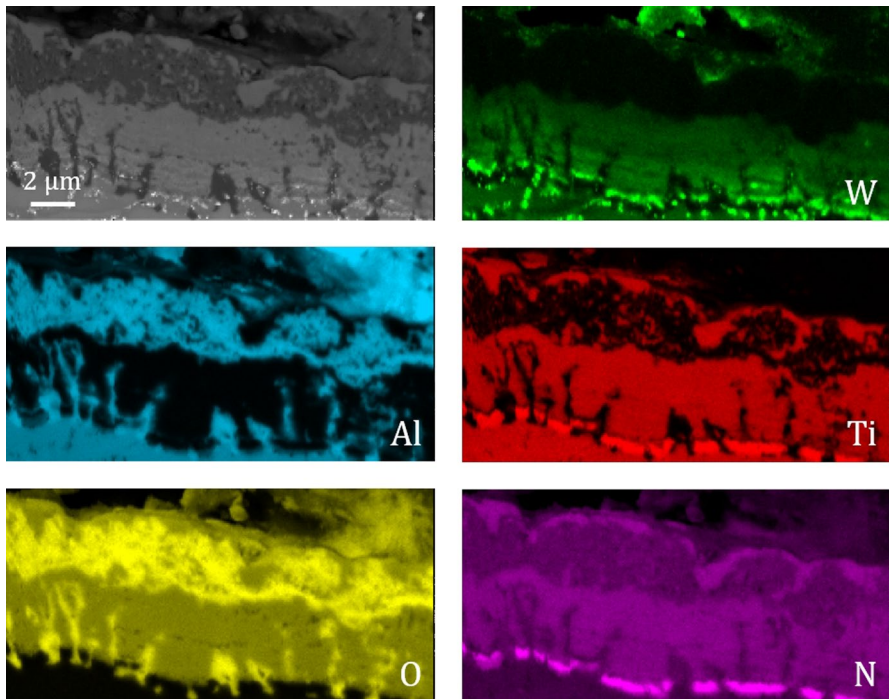
Fig. 7 SEM-BSE image and X-ray maps of the reaction product on the IRIS alloy after 1000 cycles in air at 800 °C

and Al_2O_3 is present at the metal/oxide interface. A layer with composition close to $TiAl_2$ is observed below the scale.

In addition, W-rich particles are present in the lower part of the scale (in the $TiO_2 + Al_2O_3$, $TiN + Al_2O_3$ and $TiAl_2$ layers). These precipitates are coarser than the α_2 lamella in the base alloy. However, as seen in Fig. 4, they are aligned with

the lamellar colonies. This microstructure suggests that the scale be divided into an inward-growing lower part and an outward-growing upper part, as discussed subsequently.

In summary, the sequence of layers observed in the IRIS alloy oxidized 100 h at 800 °C in air is as follows (from gas to alloy): TiO_2/porous Al_2O_3/$TiO_2 + Al_2O_3$/TiN $+ Al_2O_3 + W$/$TiAl_2 + W$/TiAl.

Cyclic Oxidation in Air

The mass gains recorded during cyclic oxidation in air at 800 °C are plotted in Fig. 5, where the results of the 240 h isothermal TGA test are also included for comparison. Although the mass gains of the cyclic test are slightly lower than those of the isothermal test, the two series are on a similar long-term trend. In the cyclic exposure, no evidence of cracking or spalling is observed from the mass gain curve or from the photographs taken at each cycle (see last photograph in insert of Fig. 5): the oxide scale appears to be continuous and intact. It is noted that the IRIS alloy meets the benchmark criterion of a maximum mass gain of 1 mg cm^{-2} after 1000 cycles in an oxidizing environment set by Pflumm et al. [9].

The morphology and elemental distribution of the reaction products formed after 1000 cycles are shown in Figs. 6 and 7, respectively. The scale has a similar constitution to that observed after 100 h. With the longer exposure time, the thicknesses of the outer Al_2O_3 layer and of the mixed $TiO_2–Al_2O_3$ layer have increased, while the Al_2O_3 grains in the mixed layer have taken a more elongated, chimney shape. The TiN layer, however, has not visibly thickened. Furthermore, $TiAl_2$ is no longer present below the TiN layer.

As seen in Figs. 6 and 7, W is present both as coarse particles (especially at the alloy/TiN and TiN/TiO_2 interfaces) and as finer particles within the Al_2O_3 chimneys and within the TiO_2. The distribution of W in the reaction product was examined in more details by TEM. Figure 8 presents HAADF images at three positions: (a) in
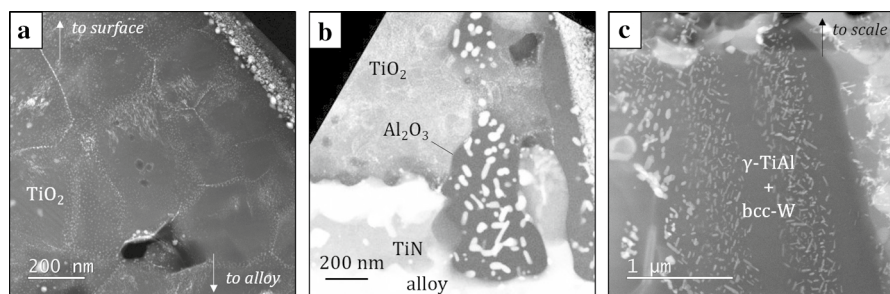
Fig. 8 STEM-HAADF images of the reaction product formed on the IRIS alloy after 1000 cycles in air at 800 °C. **a** TiO_2 grains in the TiO_2–Al_2O_3 layer with intergranular W-rich particles (see also supplementary material S1), **b** Al_2O_3 chimney across the TiN/TiO_2 interface with intragranular W-rich particles, **c** alloy near the alloy/scale interface, showing that the α_2 lamellae have been destabilized and converted to fine bcc-W particles

TiO$_2$ in the mixed TiO$_2$–Al$_2$O$_3$ layer, (b) in an Al$_2$O$_3$ chimney and (c) in the alloy immediately below the scale. All three images show bright precipitates, which suggest the segregation of a heavy element since the contrast in HAADF is related to the average atomic number. Indeed STEM/EDS analysis performed in each region (not shown here) has confirmed that the precipitates were made of W. Images were also recorded at different tilt angles to better appreciate the volume distribution of the particles. The sequence recorded in the TiO$_2$ is shown in supplementary material S1. It reveals that the W-rich particles (diameter < 6 nm) are indeed present at the TiO$_2$ grain boundaries across the foil and that the surface area fraction of these particles in the grain boundary planes is significant. As noted in "Isothermal Oxidation in Air" section after 100-h reaction, the W-rich particles in the lower part of the scale are aligned with the α_2 lamellae in the base alloy. Away from the surface, this lamellar microstructure is retained after 1000 h at 800 °C (not shown here). However, Fig. 8b and c show that the α_2 lamellae are destabilized and form discrete particles ahead of the oxidation front, which then become integrated in the Al$_2$O$_3$ chimneys.
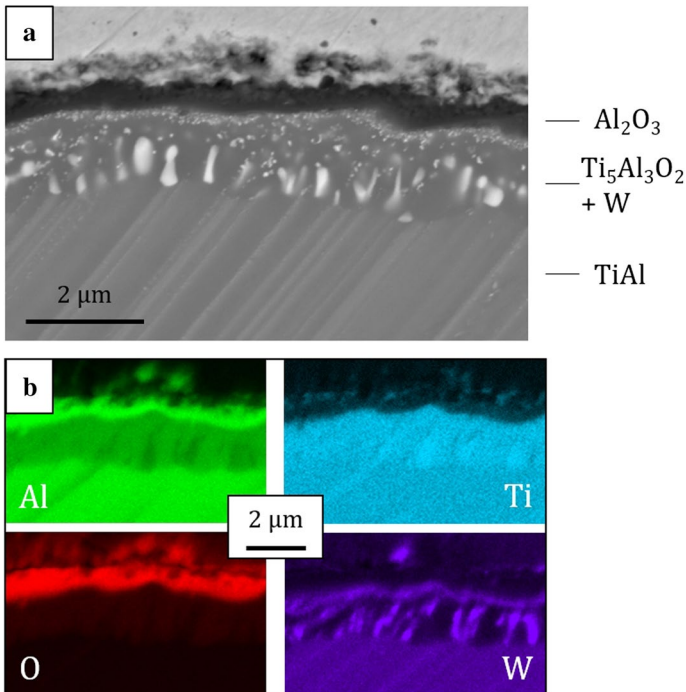
Fig. 9 SEM analysis of the IRIS alloy after 100-h oxidation in Ar-21O$_2$ at 800 °C. **a** BSE view; **b** X-ray maps

Isothermal Oxidation in Ar-21O$_2$

The mass gain recorded during isothermal oxidation of the IRIS alloy in Ar-21O$_2$ is shown together with that recorded in air in Fig. 3. Oxidation is observed to be significantly slower in the N-free gas. After an initial stage of continuous decrease, the parabolic constant stabilizes: Eq. (1) yields $k_p = 7 \times 10^{-15}$ g^2 cm^{-4} s^{-1} in the [60 h, 100 h] time range. This is about 13 times lower than the value measured in air.

Figure 9a shows a cross section of the sample after 100-h oxidation in Ar-21O$_2$. The oxidation products were determined from a combination of chemical (Fig. 9b) and crystallographic analysis (XRD pattern included in Fig. 2). The alloy formed an external α-Al$_2$O$_3$ scale and a layer of Ti$_5$Al$_3$O$_2$ at the alloy surface. Tungsten is present both as coarse particles in the Ti$_5$Al$_3$O$_2$ layer and as finer particles at the Ti$_5$Al$_3$O$_2$/Al$_2$O$_3$ interface.

Discussion

The oxidation behavior of TiAl alloys in air has been extensively studied, e.g., in Refs. [10–13], and is briefly summarized as follows. Initially, the selective oxidation of Al results in Al depletion in the metal subsurface zone. When a critical concentration is reached, Ti oxidizes; TiO$_2$ particles form at the surface of the growing Al$_2$O$_3$, which eventually leads to an outer TiO$_2$ layer on a porous Al$_2$O$_3$ layer. In parallel, Ti nitrides form at the alloy surface. The consumption of Ti causes an increase in the Al concentration, until Al$_2$O$_3$ (or Al oxy-nitride) can form again. As the oxidation front progresses, the TiN is oxidized into TiO$_2$, leading to the formation of the inner mixed TiO$_2$ + Al$_2$O$_3$ layer. Alternate sequences of Al reaction/Ti enrichment and Ti reaction/Al enrichment initially produce linear oxidation kinetics, before a steady-state is reached.

The present discussion addresses the oxidation of the IRIS alloy in relation to its composition (in particular, the presence of W) and microstructure. It first deals with W effects on the scale morphology and subscale phase transformations, before turning to the role of N in the reaction process.

Scale Morphology

The oxide scales observed here after 100 h and 1000 cycles in air (Figs. 4 and 6) are similar to those described by previous investigators for TiAl alloys, as they are constituted of TiO$_2$ and Al$_2$O$_3$ outer layers, a mixed TiO$_2$ + Al$_2$O$_3$ layer, and a layer of TiN and Al$_2$O$_3$. A major difference in the present work, evidently, is the presence of W. As illustrated in Figs. 4 and 6, W-rich precipitates are found within the Al$_2$O$_3$ chimneys, aligned with the α$_2$ lamella present in the substrate. This reflects the inward progression of the reaction front, first by selective nitridation of Ti (to form TiN) and oxidation of Al (into Al$_2$O$_3$), then by conversion of the TiN + Al$_2$O$_3$ layer into TiO$_2$ + Al$_2$O$_3$. From the comparison of Figs. 4 and 6, it can be deduced that during the parabolic oxidation stage, the thickness of the TiN + Al$_2$O$_3$ layer

remained approximately constant, while the other layers grew thicker: this shows that the two processes, nitridation and nitride conversion to oxide, tend to progress at similar rates. The nitridation/oxidation process is observed to reject W, which is found in the Al_2O_3 chimneys, as noted above, but also within the TiO_2 in the TiO_2 + Al_2O_3 layer. Rutile is known to dissolve W, which substitutes for Ti^{4+} [14]. Here, this solubility was visibly exceeded, as the TiO_2 also contained significant amounts of intergranular W-rich precipitates (Fig. 8a and supplementary material S1).

It is noted that the W-rich precipitates found in the subsurface alloy and in the TiN + Al_2O_3 and TiO_2 + Al_2O_3 layers were primarily identified based on chemical analysis by EDS. However, within Al_2O_3 and TiO_2, the precipitates were too small to determine whether they were W-rich metal or oxide, even by TEM. As noted in "Isothermal Oxidation in Air" section, a cubic phase was detected by XRD after the 100-h isothermal experiment, and indexed as bcc-W. The material analyzed by XRD includes all oxidation products, with no information as to the location of the phases. In summary, the EDS and XRD results available at this stage are not sufficient to identify the W-rich precipitates formed in the oxidation products as either W-rich metal or oxide. The dissociation pressure of WO_2 on pure W is calculated to be 10^{-19} atm at 800 °C, using Thermo-Calc [15] and the TCTI1 database. This is higher than the dissociation pressures of Al_2O_3 and TiO_2 ($p_{O_2}(Al/Al_2O_3) = 10^{-44}$ atm and $p_{O_2}(Ti/TiO_2) = 10^{-35}$ atm, also calculated with TCTI1). It is concluded that the W-rich precipitates are metallic within the alloy, the Al_2O_3 chimneys and a lower part of the TiO_2 + Al_2O_3 layer, and that they are converted to W-rich oxide within the oxide scale, at a depth where the p_{O_2} is sufficiently high. Further TEM analysis is planned to confirm.

Tungsten has been found by previous investigators to be quite effective in reducing the oxidation rate of TiAl alloys (see review in Ref. [8]). This beneficial effect has been attributed to a decrease in the rate of TiO_2 growth due to W doping [16, 17] and to the reduction of O solubility in the alloy [3, 16], which would then favor the transition from internal to external Al_2O_3 formation. In the present work, Al_2O_3 was found as vertically elongated particles ("chimneys") in the lower part of the scale and did not prevent the oxidation of Ti. Instead, it is argued that W significantly hindered the growth of the mixed Al_2O_3 + TiO_2 layer by slowing down diffusion in TiO_2 via a doping effect, possibly in the bulk and most likely at grain boundaries, where the oxide was found to be saturated with W.

Subsurface Phase Transformations

Another aspect of interest concerns the presence of an Al-enriched $TiAl_2$ layer at the alloy surface. The Al enrichment is due to the selective reaction of Ti with N to form Ti-rich nitrides (TiN and possibly some Ti_2AlN, Fig. 2). More generally, the subsurface alloy composition reflects the mass balance in the oxide + nitride scale, which appears, as a whole, to be enriched in Ti with respect to the bulk alloy composition. Whether a new intermetallic phase precipitates or not also depends on how fast interdiffusion in the alloy can proceed and accommodate composition variations. Here, the presence of $TiAl_2$ after 100 h indicates that the Al excess is initially

produced more rapidly than it can be removed; its absence after 1000 cycles shows that nitridation has slowed down. Even then, the alloy near-surface region remains richer in Al than the bulk. This is reflected in the subsurface microstructure, as the α_2 lamellae have been destabilized and replaced by bcc-W (Figs. 6 and 8c). Phase equilibrium data in Ti–Al–W at 800 °C are scarce, but our observations suggest that in a $\alpha_2 + \gamma$ mixture, W preferentially partitions to α_2, and that the oxidation-induced $\alpha_2 \rightarrow \gamma$ transformation results in W supersaturation. Further phase composition analysis is in progress, and a more detailed description of subsurface phase transformations will be published subsequently.

In previous studies of γ-TiAl oxidation, the alloy surface has typically been found to be enriched in Ti, not in Al [10–12]. Cases of Al enrichment have been reported in the literature, but in situations where TiAl was reacted in N_2 gas and nitridation was prevalent [18, 19]. As discussed by Becker et al. [18], the composition in the subsurface depends on the balance between nitridation, which preferentially consumes Ti, and oxidation, which preferentially consumes Al. When binary TiAl alloys are reacted in air, oxidation usually prevails and, even though the oxidation product contains both TiO_2 and Al_2O_3, the subsurface is Al-depleted. The different behavior observed here is presumably related to the effect of W discussed above: as the growth of the mixed $Al_2O_3 + TiO_2$ layer is slowed down, the rate of oxidation is reduced relative to that of nitridation, and as a result the mass balance is shifted toward Al enrichment.

Role of Nitrogen

Finally, it is worthwhile noting that the role of N and nitridation, which was found by previous investigators to play an important role in the oxidation behavior of TiAl alloys in air [10–12], also appears to be critical with the W-containing IRIS alloy. Indeed, oxidation in the N-free $Ar-21O_2$ mixture produced a slow-growing Al_2O_3 scale and prevented the reaction of Ti altogether (Fig. 9). The $Ti_5Al_3O_2$ phase growing at the alloy surface contributes to the weight gain and precludes a direct comparison with other alloy systems based on thermogravimetric data. However, if their results are converted to Al_2O_3 thickness, the scale thickness observed here is comparable to that of transient (θ and γ) Al_2O_3 grown on β-NiAl at 800 °C in Refs [20, 21].

Conclusion

The IRIS alloy, Ti–48Al–2W–0.1B (at. %) consolidated by SPS, presents a relatively good oxidation resistance in air at 800 °C, with a parabolic constant of 9×10^{-14} g^2 cm^{-4} s^{-1}. Furthermore, the oxide scale presents no cracking or spalling after 1000 cycles (1167 h) of oxidation at this temperature.

The oxide scale formed in air contains layers of TiO_2, Al_2O_3, $TiO_2 + Al_2O_3$ and $TiN + Al_2O_3$. Tungsten is rejected by the nitridation and oxidation reactions and is found within TiO_2 in the $TiO_2 + Al_2O_3$ layer and as bcc-W particles in the

$TiN + Al_2O_3$ layer. In particular, significant amounts of W-rich precipitates are present at the grain boundaries of the TiO_2. The beneficial effect of W is attributed to a reduction in the growth rate of the $TiO_2 + Al_2O_3$ layer, due to reduced diffusion rates in the W-doped TiO_2. As a result, the subsurface alloy is enriched in Al, compared to the bulk, to a point where $TiAl_2$ is formed underneath the scale. Nitridation is found to have a critical role in the reaction mechanism, as oxidation in $Ar-21O_2$ results in external Al_2O_3 formation and prevents the reaction of Ti.

Compliance with Ethical Standards

Conflict of interest The authors declare that they have no conflict of interest.

References

1. T. Voisin, J.-P. Monchoux, L. Durand, N. Karnatak, M. Thomas and A. Couret, *Advanced Engineering Materials* **17**, 2015 (1408–1413). https://doi.org/10.1002/adem.201500019.
2. M. Thomas and M. P. Bacos, *AerospaceLab* **3**, 2011 (1–11).
3. Y. Shida and H. Anada, *Corrosion Science* **35**, 1993 (945–953). https://doi.org/10.1016/0010-938X(93)90313-6.
4. T. Voisin, J.-P. Monchoux, M. Perrut and A. Couret, *Intermetallics* **71**, 2016 (88–97). https://doi.org/10.1016/j.intermet.2016.01.003.
5. R. Pflumm, A. Donchev, S. Mayer, H. Clemens and M. Schütze, *Intermetallics* **53**, 2014 (45–55). https://doi.org/10.1016/j.intermet.2014.04.010.
6. A. Donchev, M. Galetz, S. Mayer, H. Clemens and M. Schütze, *MRS Advances* **2**, 2017 (1361–1367). https://doi.org/10.1557/adv.2017.170.
7. D. Monceau and B. Pieraggi, *Oxidation of Metals* **50**, 1998 (477–493). https://doi.org/10.1023/a:1018860909826.
8. J. W. Fergus, *Materials Science and Engineering: A* **338**, 2002 (108–125). https://doi.org/10.1016/S0921-5093(02)00064-3.
9. R. Pflumm, S. Friedle and M. Schütze, *Intermetallics* **56**, 2015 (1–14). https://doi.org/10.1016/j.intermet.2014.08.002.
10. A. Rahmel, M. Schütze and W. J. Quadakkers, *Materials and Corrosion* **46**, 1995 (271–285). https://doi.org/10.1002/maco.19950460503.
11. C. Lang and M. Schütze, *Materials and Corrosion* **48**, 1997 (13–22). https://doi.org/10.1002/maco.19970480104.
12. F. Dettenwanger, E. Schumann, M. Ruhle, J. Rakowski and G. H. Meier, *Oxidation of Metals* **50**, 1998 (269–307). https://doi.org/10.1023/A:1018892422121.
13. V. Maurice, G. Despert, S. Zanna, P. Josso, M.-P. Bacos and P. Marcus, *Acta Materialia* **55**, 2007 (3315–3325). https://doi.org/10.1016/j.actamat.2007.01.030.
14. J. Graham and R. C. Morris, *Mineralogical Magazine* **39**, 1973 (470–473).
15. J.-O. Andersson, T. Helander, L. Höglund, P. Shi and B. Sundman, *Calphad* **26**, 2002 (273–312). https://doi.org/10.1016/S0364-5916(02)00037-8.
16. Y. Shida and H. Anada, *Oxidation of Metals* **45**, 1996 (197–219). https://doi.org/10.1007/BF01046826.

17. S. A. Kekare and P. B. Aswath, *Journal of Materials Science* **32**, 1997 (2485–2499). https://doi.org/10.1023/A:1018529829167.
18. S. Becker, A. Rahmel, M. Schorr and M. Schütze, *Oxidation of Metals* **38**, 1992 (425–464). https://doi.org/10.1007/BF00665663.
19. J. Magnan, G. C. Weatherly and M.-C. Cheynet, *Metallurgical and Materials Transactions A* **30**, 1999 (19–29). https://doi.org/10.1007/s11661-999-0192-8.
20. G. C. Rybicki and J. L. Smialek, *Oxidation of Metals* **31**, 1989 (275–304). https://doi.org/10.1007/bf00846690.
21. M. W. Brumm and H. J. Grabke, *Corrosion Science* **33**, 1992 (1677–1690). https://doi.org/10.1016/0010-938x(92)90002-k.

Publisher's Note Springer Nature remains neutral with regard to jurisdictional claims in published maps and institutional affiliations.